

This work was written as part of one of the author's official duties as an Employee of the United States Government and is therefore a work of the United States Government. In accordance with 17 U.S.C. 105, no copyright protection is available for such works under U.S. Law.

Public Domain Mark 1.0

<https://creativecommons.org/publicdomain/mark/1.0/>

Access to this work was provided by the University of Maryland, Baltimore County (UMBC) ScholarWorks@UMBC digital repository on the Maryland Shared Open Access (MD-SOAR) platform.

Please provide feedback

Please support the ScholarWorks@UMBC repository by emailing scholarworks-group@umbc.edu and telling us what having access to this work means to you and why it's important to you. Thank you.

JGR Space Physics



TECHNICAL REPORTS: METHODS

10.1029/2020JA028960

Key Points:

- Scale factors to adjust a background photoelectron map for low-energy top-hat electron ESAs should be updated multiple times per month
- A method is presented to use proxy spectral irradiances to estimate the scale factor
- Three wavelengths suitable for use as proxies with this method are found

Correspondence to:

D. da Silva,
daniel.e.dasilva@nasa.gov

Citation:

da Silva, D., Gershman, D., Barrie, A., Elkington, S., Li, X., Kirk, M., et al. (2021). Three solar irradiance proxies for aperture photoelectron detections in top-hat ESAs coated with Ebonol-C. *Journal of Geophysical Research: Space Physics*, 126, e2020JA028960. <https://doi.org/10.1029/2020JA028960>

Received 20 NOV 2020
Accepted 26 NOV 2021

Three Solar Irradiance Proxies for Aperture Photoelectron Detections in Top-Hat ESAs Coated With Ebonol-C

D. da Silva^{1,2,3} , D. Gershman¹ , A. Barrie^{1,4} , S. Elkington² , X. Li², M. Kirk^{1,5} , B. Giles¹ , L. Avano^{1,6} , J. Shuster^{1,6} , B. Paterson¹ , C. Schiff¹, and L. J. Chen¹ 

¹NASA Goddard Spaceflight Center, Greenbelt, MD, USA, ²Laboratory for Atmospheric and Space Physics, University of Colorado Boulder, Boulder, CO, USA, ³Goddard Planetary Heliophysics Institute, University of Maryland, Baltimore County, Baltimore, MD, USA, ⁴Aurora Engineering, Orono, ME, USA, ⁵Atmosphere and Space Technology Research Associates (ASTRA) LLC, Louisville, CO, USA, ⁶Goddard Planetary Heliophysics Institute, University of Maryland, College Park, MD, USA

Abstract Decades after the introduction of top-hat electrostatic analyzers (ESAs) to experimental space plasma physics, photoelectron noise in apertures of low-energy electron instruments continues to be an issue in instrument performance. The photoelectrons at each portion of measured phase space distribution can be mapped through laboratory and in-flight testing, and have been for many missions. In flight, the photoelectrons are a response to dynamic solar EUV spectral intensities which vary over the course of a solar cycle and even within a solar rotation. This paper outlines three solar irradiance proxies that can be used to scale a map of photo-electron locations in phase space in order to account for dynamic solar activity. These proxies apply to top-hat ESAs coated with Ebonol-C (the most common coating) used by missions such as MMS, Solar Orbiter, the Van Allen Probes, and Juno. These proxies are discovered by searching possible wavelengths for correlation with an independent algorithm for MMS/FPI (Magnetospheric Multiscale Mission/Fast Plasma Instrument) which automatically determines the scaling factor. The three wavelengths that serve as viable proxies are found to be: 17.5, 30.5, and 37.5 nm.

Plain Language Summary Space instruments measuring electron distributions have a noise source originating from photoelectrons caused by solar EUV. The photoelectrons are closely associated with the spectrum of solar EUV, which is dynamic over a solar cycle and even within a solar rotation. This work shows that three wavelengths (17.5, 30.5, and 37.5 nm) serve as good proxies for the entire relevant EUV spectrum that generates the noise associated with the photoelectrons. These proxy wavelengths work well when the instrument is a top-hat electrostatic analyzer (ESA) coated with Ebonol-C, which is a commonly used coating.

1. Introduction

Top-hat electrostatic analyzers (ESAs) have an aperture open to space which allows for incoming particles to enter the instrument. As the aperture spins into sunlight, solar UV irradiance excites the exposed metal surface which emits photoelectrons into the instrument. As the ESA scans over the instrument's energy range, time spent in the low-energy range allows for these photoelectrons to pass through the energy filter for detection. A visual depiction of the solar EUV photons illuminating an instrument aperture can be found in Figure 1, where one can note how the photoelectrons will appear prior to the energy-filtering optics. In scientific studies, photoelectrons appear in spectrograms or velocity distribution plots as a nearly constant low-energy population always present (while exposed to sunlight) regardless of the ambient plasma populations. A set of example spectrograms with the photoelectrons highlighted can be found in Figure 2, taken from the dayside magnetosphere at GSE $X \approx 11$ Re. In the highlighted part of this interval, it can be seen that there is a low-energy electron population where there is no low-energy ion population, which confirms the non-ambient nature of the population.

As the spacecraft spins in front an illumination source, the locations in which aperture photoelectrons appear in the phase space distribution have been mapped through on-ground and in-flight testing. The angle between the sunline and the instrument outward facing vector is known as the sun-analyzer angle (Figure 1). Experimentation from ground testing using an artificial illumination source revealed a characteristic artifact in ESAs; the apparent photoelectron rate over sun-analyzer angles is double-peaked due to optics shaping and declines with energy (Carlson et al., 1998). This characteristic artifact was confirmed during flight with true solar illumination

©2021. The Authors.

This is an open access article under the terms of the [Creative Commons Attribution License](https://creativecommons.org/licenses/by/4.0/), which permits use, distribution and reproduction in any medium, provided the original work is properly cited.

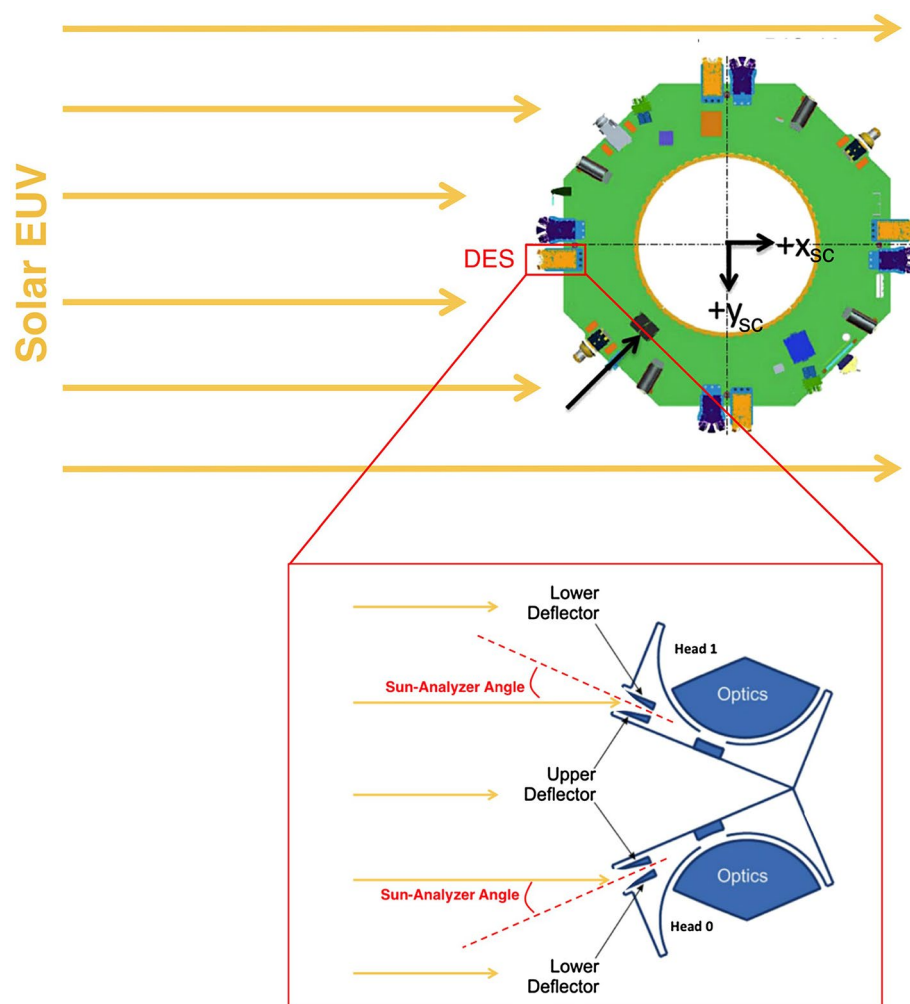


Figure 1. Example of solar illumination into a dual-head top-hat ESA instrument aperture (in this case, the Dual Electron Spectrometer from a Magnetospheric Multiscale Mission spacecraft). This image is reprinted with permission from Gershman et al. (2017).

during the Time History of Events and Macroscale Interactions during Substorms (THEMIS) mission (McFadden et al., 2008), and once again during the Magnetospheric Multiscale (MMS) mission's Fast Plasma Investigation (FPI) (Burch et al., 2016; Gershman et al., 2017; Pollock et al., 2016).

The photoelectron bias in the electron measurement also effects moments calculated from the phase space distribution. With an added population on the sun-facing side, the density will increase, and the bulk velocity will be skewed in the direction away from the sun. This is especially problematic in regions where the count rate originating from ambient plasma is comparable to the count rate originating from photoemission.

On the MMS FPI instrument, the photoelectron bias was shown to bias the anti-sunward electron bulk velocity by an amount on the order of 10%–50% before being addressed (Gershman et al., 2017). To address the bias, a method for collecting the photoelectron map on top of the electron phase space distribution using observation from the night-side plasma sheet was practiced during the MMS mission. This method scales a photoelectron map to account for varying solar EUV intensity, before subtracting it off the electron counts converted to phase space distribution. The significant drawback of this method of determining the scale factor is that it is tied to the presence of an ion sensor and the MMS mission's orbit.

Top hat ESAs are coated with high work function materials that reduce the photoemission rate to minimize the production of photoelectrons. The application of these materials is sometimes called “blackening.” Without this

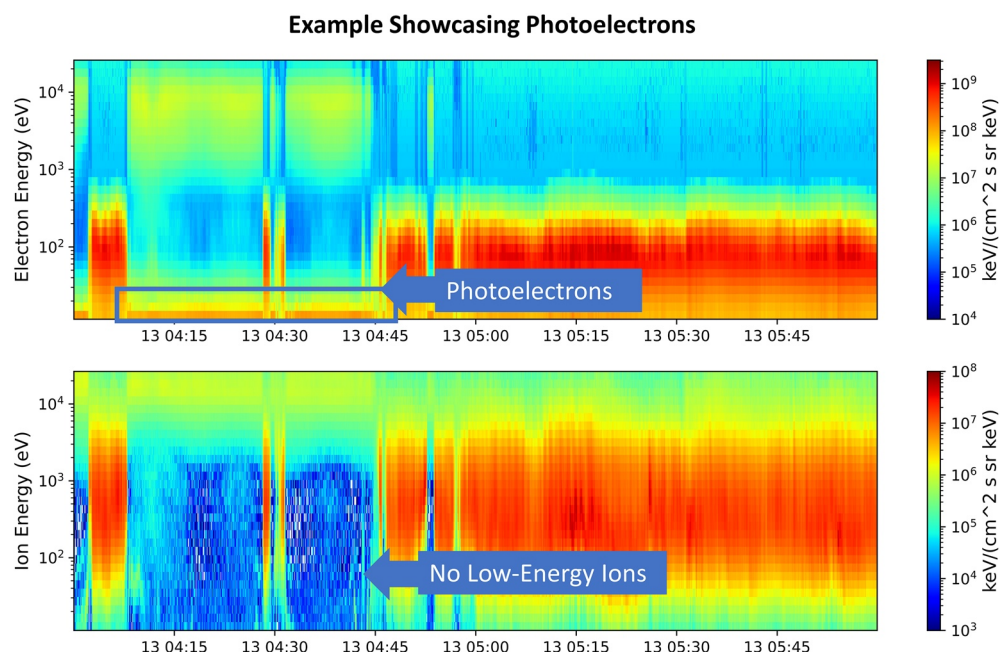


Figure 2. Example data showcasing an isolated photoelectron population. This interval was taken from MMS FPI data on 13 November 2015 in the dayside magnetosphere (GSE $X \approx 11$ Re). The photoelectrons are understood not to be from the ambient environment due to the lack of low-energy ions.

coating, the photoelectron bias would be significantly under addressed. The most common of these coatings is Ebonol-C, used by the MMS mission's Fast Plasma Investigation, Solar Orbiter's Solar Wind Analyzer (Mueller et al., 2013; Owen et al., 2020), the Van Allen Probes (Funsten et al., 2013; Mauk et al., 2013), and Juno (Bolten et al., 2017; McComas et al., 2017). Ebonol-C is known to be thermodynamically stable without the tendency to recrystallize, evolve, or revert to other compounds (Harris, 1948).

Adding to the complexity of the problem, the formation dynamics of the solar EUV spectrum that relates to the scale factor is multifaceted and varies by orders of magnitude on time scales of the years/decades of a solar cycle, days/months of a solar rotation, and the minutes/hours of solar flares (NOAA Space Weather Prediction Center, 2021). The EUV spectrum of the sun originates in a wide range of environments in the corona, transition region, and chromosphere. Furthermore different parts of the solar EUV spectrum grow and diminish independently during these time scales. Consistently over the course of the solar cycle, large-scale changes in the dynamics of the sun alter the EUV emissions, and during a solar rotation the EUV that reaches the spacecraft varies as surface features come in and out of view (Kivelson & Russell, 1997; Priest, 2012). Work on the related topic of solar cycle EUV variation and spacecraft charging has undertaken with Cluster mission (Lybakk et al., 2012), and on the Pioneer mission to Venus (Brace et al., 1988). This paper does not deal with a flaring sun because their impulsive changes are dynamic and vary widely between types of flares, instead focusing on solar cycle and solar rotation effects as they are both more regular changes to the solar EUV irradiance.

The approach used by this paper is to develop a simplified method for photoelectron removal. A full, detailed description of the changing solar EUV input would require inputs from all wavelengths in the EUV range and would be both difficult to validate and manage. Instead, we identify several solar spectral irradiance proxies identified to be representative of the spectrum and subtract an amount of the photoelectron map set by a baseline level of one of these proxies. Each one of these proxies is sufficient to represent the total EUV spectrum, without needing to model the entire solar EUV spectrum.

In section *Solar Irradiance Proxies for Aperture Photoelectron Detections*, we describe the methodology for applying each of the proxies to photoelectron removal. In *Case Study with MMS/FPI* section, we summarize the progress made in photoelectron removal and the application to future mission operations. For those curious about the methodology undertaken to establish the validity of these wavelengths as proxies, the full details can be found in Appendix A.

2. Solar Irradiance Proxies for Aperture Photoelectron Detections

Photoelectron removal subtracts off a background photoelectron map following the measurement's conversion from counts to phase space distribution. This can be summarized by the following equation, where $f_{e,final}$ is the final calibrated electron phase space distribution after removal is applied, $f_{e,initial}$ is the initial measured electron phase space distribution before removal is applied, f_{photo} is the photoelectron map (normalized to unit density), and n_{photo} is a scale factor that adjusts for the amount of the map to remove. This scale factor can change by up to an order of magnitude on timescales of a solar cycle (~ 11 years) and solar rotation (~ 27 days).

$$f_{e,final} = f_{e,initial} - f_{photo} * n_{photo} \quad (1)$$

This paper reports new single-wavelength proxies that can be used to obtain the scale factor (n_{photo}) for the photoelectron map with a top hat ESA coated with Ebonol-C. This method works in scenarios where the method of Gershman et al. (2017) for determining the scale factor based on paired ion data are not possible, for example, due to non-existing or insufficient ion measurements. These wavelengths proxies (λ) are used in the following scale factor equation (Equation 2), where the function $n_{photo}(t)$ is the target scale factor to be used at a time t , the variable $I_{\lambda}(t)$ is a spectral irradiance input at time t , the quantity $n_{photo}(t_0)$ is the base scale factor a reference time point early on in the mission, and $I_{\lambda}(t_0)$ is the spectral irradiance at the reference point. The three wavelengths that may be used for λ are: 17.5, 30.5, and 37.5 nm.

Normally, the photoelectron map is collected during the commissioning stage when the instrument is checked out and calibrated before start of the primary mission, but after initial outgassing effects are complete. In Gershman et al. (2017), the MMS photo-electron map was normalized to 1, and in following this convention the variable $n_{photo}(t_0)$ serves as a base de-normalizing scale factor.

$$n_{photo}(t) = \frac{I_{\lambda}(t)}{I_{\lambda}(t_0)} n_{photo}(t_0) \quad (2)$$

This equation only works when $I_{\lambda}(t)$ is effectively *directly proportional* to the total solar input covering multiple wavelengths that generates the photoemission. For generic variables X and Y to be directly proportional (i.e., $Y \propto X$), it is sufficient to establish that $Y = aX$ for some a . Using spacecraft data, this can be established by confirming a strong linear regression model of $Y = aX + b$ holds and yields $b \approx 0$ after fitting. When this is done, the regression equation reduces to $Y = aX$ and the required condition is met for direct correlation. The special condition of a linear correlation with no intercept for these proxies was established for about four years of data during the decline of solar cycle 24 (late 2015–late 2019).

To prepare an instrument during commissioning for aperture photoelectron removal, we collect and normalize a photoelectron map in the night-side plasma sheet. This region is used because the ambient electron fluxes occur well above the photoelectron signal, allowing the two populations to be cleanly separated. The solar spectral irradiance for the chosen proxy wavelength $I_{\lambda}(t_0)$ at that time and region is observed, as well as the scale factor $n_{photo}(t_0)$ to undo normalization. At future times, the background photoelectrons can be subtracted from the measured phase space distribution the method given by Equation 1 and the amount to subtract off to account is given using the scale factor $n_{photo}(t)$ in Equation 2. The spectral irradiance, $I_{\lambda}(t_0)$, used can be from a direct instrument measurement from another satellite or from a model—whichever yields the best confidence.

3. Case Study With MMS/FPI

We apply the bias correction method outlined in the previous section to data from MMS/FPI in order to observe the subtle effects captured by using irradiance data. The calibration scale factor n_{photo} used in the data released by the MMS mission and the calibration factors estimated by the irradiance method in the previous section (one for each of the three proxy wavelengths) are compared in Figure 3. The values labeled as released in FPI data were taken from the header of the Level 2 Common Data Format (CDF) files released by the mission.

There is good agreement between the scale factor used in released FPI data and the scale factor estimated by the irradiance method. In both, there is a decline over time attributable to understood solar cycle effects. Variation in (E)UV output over a solar cycle has been observed for multiple cycles, recently from Solar Cycles 21 and 22 (Mahajan et al., 1998) and Solar Cycle 23 (Del Zanna & Andretta, 2011). Fine-grained features appear in the

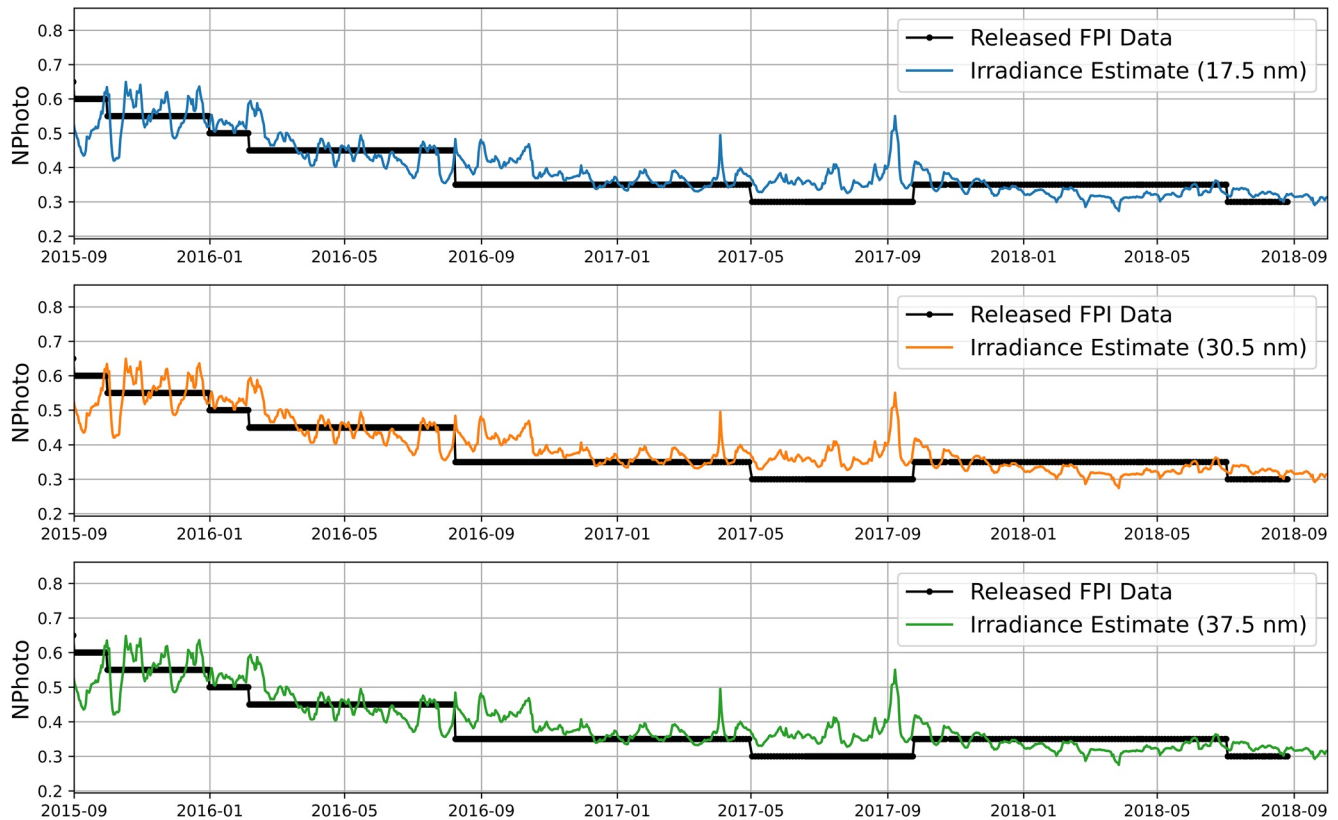


Figure 3. Plot of the coarse photoelectron scale factor (n_{photo}) used in the data released by the FPI mission compared to finer-grained versions estimated by the irradiance method outlined in this paper. This plot begins in solar maximum and leads into the decline to solar minimum. The overall decline in the scale factors present in all curves is consistent with the understood decline in solar EUV output during these phases of a solar cycle. In these plots variation in the irradiance estimates on the order of a solar rotation can be seen that capture another understood solar effect of high EUV regions coming in and out of view of the earth as the sun exhibits differential rotation.

irradiance estimates with a period of a solar rotation (~ 27 days), attributable to high UV solar surface features coming in and out of view of the spacecraft. The variation caused by solar features is larger in solar max than during solar minimum, consistent with solar theory (Lean et al., 1987; Rottman, 1988).

The observations of these trends in relation to solar emission were found as well on the Cluster mission (Lybekk et al., 2012) and on the Pioneer mission to Venus (Brace et al., 1988). Due to solar differential rotation features at higher latitudes will rotate in and out of view of the spacecraft more slowly than those at the equator. Changes in the spatial concentration of EUV sources on the sun between solar maximum and solar minimum lead to the variation in photoelectrons with a period of a solar rotation. Because the change in the scale factor on the time scale of a solar rotation is much greater during solar maximum than minimum, it is more critical to update the calibration scale factor with higher frequency during solar max.

We verified the solar origin of the fine-scale variability by applying a Fast Fourier Transform (FFT) to the irradiance estimate data from Figure 3. For each of wavelengths, the power frequency of the irradiance estimate data peaked at once per 26.4 days. This confirms the interpretation of the solar rotation theory because the peak in the power frequency is nearly identical to the solar synodic rotation period of 26.24 days. The remaining difference is attributed to not all active regions existing on the equator and the solar rotation slowing with increasing latitude.

To summarize, we observe two characteristic time scales in the photoelectron scale factors produced by the solar irradiance estimates that are consistent with solar theory: (a) the solar cycle (solar max yields higher photoelectron rates) and (b) the solar rotation (features appearing/disappearing from rotation, with most effect when feature concentration is highest in solar maximum).

4. Conclusion

In this paper, we present a simplified method for applying photoelectron removal using the scaled photoelectron map method established during MMS. This effect is important to all instruments measuring low-energy electrons, and even more important when measuring regions with low count rate. While applicable to small and large missions alike, it is of particular benefit to small missions such as cubesats without the funding and time resources to launch a full investigation around photoelectron removal.

We find that EUV solar irradiance at 17.5, 30.5, and 37.5 nm are ideal proxies for estimating the scale factor for photoelectron calibration.

The ability to estimate the photoelectron level is useful not only when cleaning and preparing the data for scientific consumption, but also for predicting the instrument performance in the future. Long-term solar forecast models (Petrovay, 2020) can be gauged to get a picture of these proxies years or decades into the future, and one can predict how the photoelectron bias will change at those times.

The community has not yet found a best practice for addressing photoelectron bias in the presence of a flaring sun. During these flares, short wavelength emissions above the work function will increase drastically for short time periods. With long-duration X-ray events lasting on the orders of hours, one may ask how current methods may succeed or fail under such events. Should the methods prove insufficient, the appropriate response is to either remove the data from the publicly released set or pursue a flare-specific correction. With more complex physics and dynamics, a flaring sun will be considered in future work.

In this paper, we provided an objective and robust approach to finding the required amount of photoelectron removal. It is our hope this increases the quality of scientific data for low-energy electron instruments and becomes a best practice and common convention for photoelectron removal. By having a single method for treatment of photoelectrons across as many instruments as possible, the community's understanding of new low-energy electron data is enhanced.

Appendix

A1. Introduction

In this appendix we cover the method used for determining the three proxies for Ebonol-C photoemission in top-hat electrostatic analyzers from solar output. This was done with data from the MMS mission's FPI instrument between late 2015 to late 2018, covering the decline of a solar cycle. This decline of a solar cycle is meant to be representative of the different EUV spectrums which can be output from the sun as it changes over the course of a solar cycle.

In previous work by Gershman et al. (2017) a method was outlined for determining the photoelectron scale factor through the combination of ion and electron data. We automated this algorithm and ran it over several years to gather sufficient data to do a statistical comparison with irradiance data. When sufficient data on the photoelectron scale factor was gathered, solar irradiance data was integrated through a search over candidate EUV wavelengths for those that produced a strong correlation.

The aperture photoelectron detections are considered as an additive velocity distribution on top of the ambient electron velocity distribution. This leads us to the following equations:

$$f_{e,measured} = f_{e,ambient} + f_{photo} \quad (A1)$$

$$n_{e,measured} = n_{e,ambient} + n_{photo} \quad (A2)$$

$$\vec{v}_{e,measured} = \frac{n_{e,ambient}\vec{v}_{e,ambient} + n_{photo}\vec{v}_{photo}}{n_{e,ambient} + n_{photo}} \quad (A3)$$

where subscript “e.measured” refers the measured electron quantities, “e.ambient” refers to the naturally ambient electron quantities, and “photo” refer to the photo-electron quantities. The variable n_{photo} serves doubly for us as the photoelectron scale factor for calibration, as well as the total number density of additive photoelectron population. The quantity n refers to the electron number density and the quantity v refers to the electron bulk velocity.

Equations A2 and A3 follow from Equation A1 when one integrates the number density and bulk velocity moments, respectively. In Equation A3, we point out the nature of this quantity as a weighted average weighted by the ambient and photoelectron density. When the ambient density becomes large compared to the photoelectron density, such as in the magnetosheath, the effect of the photoelectrons in the electron bulk velocity dwindles.

The method outlined by Gershman et al. (2017) to estimate n_{photo} through the combination of electron and ion data implicitly makes the assertion that the ambient ion bulk velocity equals the ambient electron bulk velocity when averaged on multi-second time-scale, and eliminates differences from current structures present in the MMS orbit ($\vec{v}_{i,ambient} = \vec{v}_{e,ambient}$). For a more detailed discussion of this at a physical level, see Gershman et al. (2017). In that work, $\vec{v}_{i,ambient}$ is the total ion bulk velocity combining both helium and hydrogen populations into one un-weighted average, and $\vec{v}_{e,ambient}$ is the total electron bulk velocity. The integration in both bulk velocities include a correction where-in the energies are adjusted by $E' = E + q\phi$ to account for the effect of spacecraft potential., where q is the unit charge, ϕ is the spacecraft potential, E is the original incident energy, and E' is the adjusted energy.

By setting $\vec{v}_{i,ambient} = \vec{v}_{e,ambient}$, we arrive at the following equation by manipulating Equation A3. This new Equation A4 can be solved to give us an estimate for the photo-electron scale factor n_{photo} as a function of the total measured electron quantities and the ambient ion bulk velocity.

$$\vec{v}_{i,measured} = \frac{n_{e,measured}\vec{v}_{e,measured} - n_{photo}\vec{v}_{photo}}{n_{e,measured} - n_{photo}} \quad (A4)$$

Because the bulk velocities are three dimensional, this yields an over-determined system of three equations and one unknown. However, \vec{v}_{photo} is only notable in the anti-sunlit direction (photoelectrons added on the sunlit side add to the bulk velocity away from the sun). This anti-sunlit direction which points toward -X in the GSE coordinate system. Therefore, this system of three equations was reduced to one equation with component along the GSE X axis.

Estimating n_{photo} with Equation A4 is most effective when $n_{e,measured}$ and n_{photo} have values on a similar scale and around 50% of each other. In the MMS orbit this is the case within the magnetosphere where particle densities are typically around $n_e \approx 1 \text{ cm}^{-3}$, but not in the magnetosheath where particle densities are typically $n_e > 5 \text{ cm}^{-3}$.

A2. Automated Estimation of n_{photo}

We created an automated tool for searching through the FPI data and determining a photoelectron scale factor from the data. The FPI Level 2 data product and associated photo-electron model available from the MMS Science Data Center is used. The data set analyzed covers three years of solar cycle decline, from which n_{photo} is calculated wherever possible.

The tool filtered out less than ideal data to get the best estimates. Data is filtered out during periods with high spacecraft potential ($> 12.5 \text{ V}$) and ion number densities less than 0.2 cm^{-3} or greater than 1 cm^{-3} . Spacecraft potential is measured on board MMS/FPI with instrumentation as part of an active spacecraft control system (Torkar et al., 2016). Data with high spacecraft potential is removed to clear out periods where externally generated photoelectrons interfered with the aperture photoelectron detections. Low densities are eliminated to remove data with a high-level of uncertainty in the bulk velocity measurement (Gershman et al., 2019) that would propagate into uncertainty in the estimate.

The algorithm produces estimates for the n_{photo} parameter for each measurement in a 2-hr FPI Level 2 Fast Survey file where the aforementioned restrictions are met. The average estimate over the 2-hr file is recorded as the nominal estimate for the whole file if the standard deviation of estimates within the file is sufficiently low (under 0.1 cm^{-3} with a minimum of 500 samples). The tool generates a plot for each file as shown in Figure A1.

In Figure A1, the top panels show the number density of the ion and electron instruments. The second panel shows the electron GSE X bulk velocity component using different levels of n_{photo} . This is to illustrate how the photoelectron scale factor n_{photo} influences the electron GSE bulk velocity after photoelectron removal. Colored lines represent the candidates for n_{photo} per the previous work done by Gershman et al., with the ideal candidate being the one that produces matching electron and ion GSE X bulk velocity (black line). The third panel shows

the n_{photo} estimate produced by the algorithm for each measurement, with a horizontal red line plotted at the average. Spread in the estimates is expected to statistical uncertainty. The fourth panel shows a histogram of the estimates to illustrate the spread. This set is a good one because the spread is low relative to others. The average estimate from the 2-hr file represented below was accepted into the final set because the estimates had a standard deviation of 0.05 cm^{-3} , less than the selection threshold.

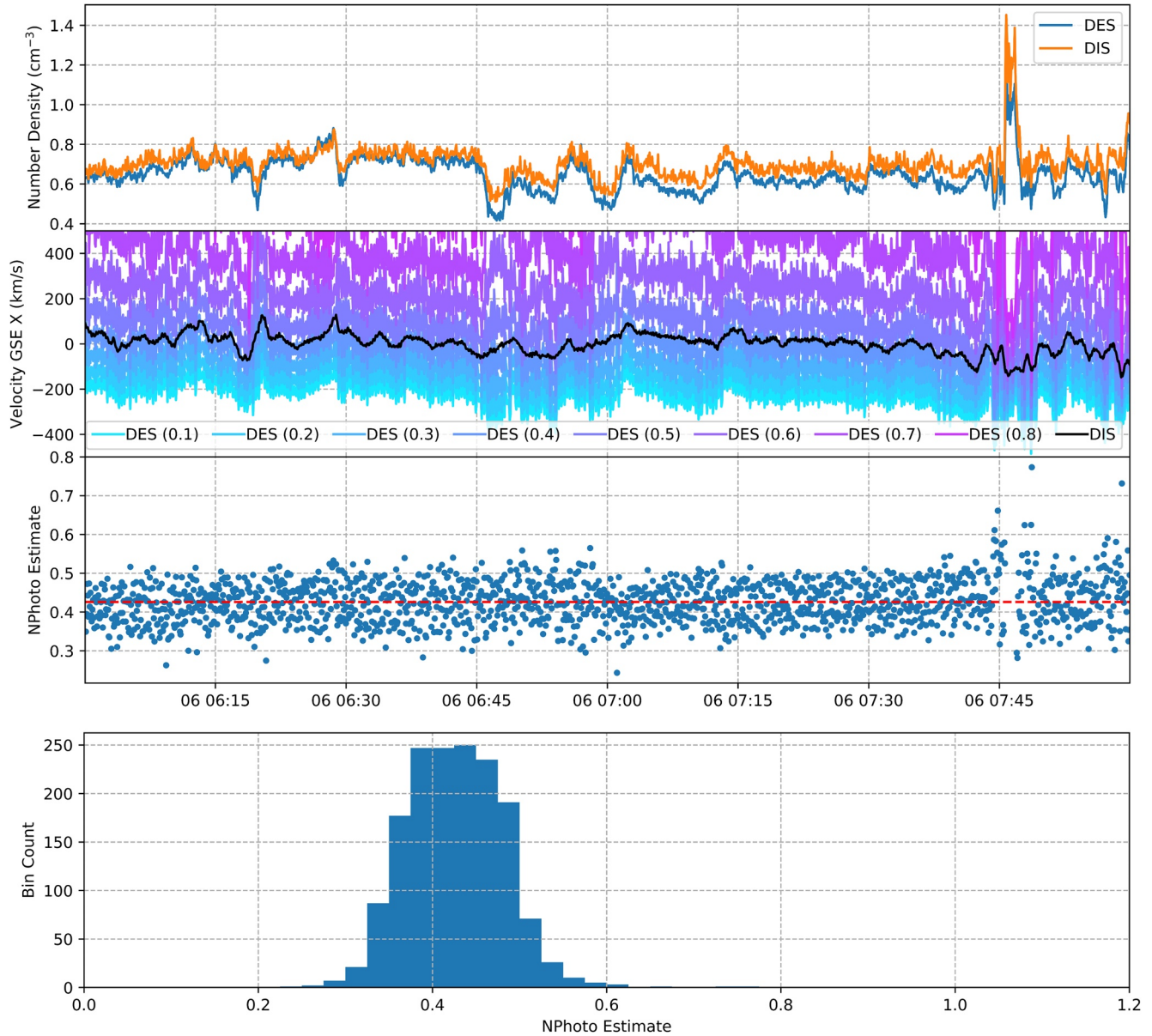


Figure A1. Output plot of the n_{photo} estimation algorithm for 2-hr duration starting at 2017-09-06 hr 6:00 from MMS1. The top panel shows the ion and electron number densities for reference. The second panel shows the ion bulk velocity and different scaled version to the electron bulk velocity for comparison. The third panel shows the photoelectron estimates at each timestep. The final fourth panel shows a histogram of the estimates. The DES acronym corresponds to the Dual Electron Spectrometer, and the DIS acronym corresponds to the Dual Ion Spectrometer, which are the electron and ion spectrometers on MMS/FPI respectively.

A3. Correlation With Candidate EUV Proxies

The data is paired with spectral irradiance data between 0.1 and 309.5 nm, as well as the F10.7 Flux. Specifically, the 0.1–39.5 nm range was taken from the SORCE/XPS instrument's Level 3 data, 40.5–115.5 nm from the TIMED/SEE instrument's L2 data, 115.5–309.5 nm from the SORCE/SOLSTICE instrument's Level 3 data, and the F10.7 Flux from NOAA's data product.

All spectral irradiance data is obtained from the CU-Boulder Laboratory for Atmospheric and Space Physics (LASP). The SORCE data is obtained with a spectral resolution of 1 nm, whereas the TIMED data is obtained with a 0.1 nm and resampled to 1 nm bins. The reader should be aware that the XPS data itself depends directly on the CHIANTI solar model and is not a direct measurement itself.

The automated photoelectron tool calculations of n_{photo} combined with these spectral irradiance measurements allows for a search for sufficient proxies in the list of spectral irradiances. The ideal proxy is one that is directly correlated to the n_{photo} estimate. This can be established by showing that a linear regression result yields a high correlation with a zero intercept. An intercept of zero is required for the method application in Equation 2 to work. To search for such a proxy, we performed regressions using the standard ordinary least squares (OLS) method.

Scatterplots of the regressed data using fits are plotted. Some of these fits are not good—they were made and plotted to show this and test the hypothesis of whether they were. It was found that there was a cluster of three wavelengths with the highest values of r^2 (>0.75) and small intercepts ($<0.025 \text{ cm}^{-3}$). These intercepts represent less than 1% of the values of n_{photo} used throughout the mission (see section *Case Study with MMS/FPI*). For these three wavelengths, the conclusion is drawn that they are appropriate proxies for the effective solar EUV spectrum. The wavelengths are: 17.5 nm, 30.5 nm, and 37.5 nm. Figure A2 shows the scatterplots and linear regressions for these irradiances. These wavelengths are tied to coronal and upper transition regions on the sun. It was found F10.7 cm radio flux served as a poor proxy, with $r^2 = 0.45$ and intercept = 0.12 cm^{-3} . The band containing Lyman-alpha also served as a poor proxy, with $r^2 = 0.78$ but an intercept = 0.76 cm^{-3} .

This statistical study was used in conjunction with an automated tool used to produce the necessary data for the statistics. The data covered the decline of a solar cycle, intended to represent the multiple EUV spectra that can occur during solar cycle evolution. These irradiances (17.5 nm, 30.5 nm, and 37.5 nm) represent an index for

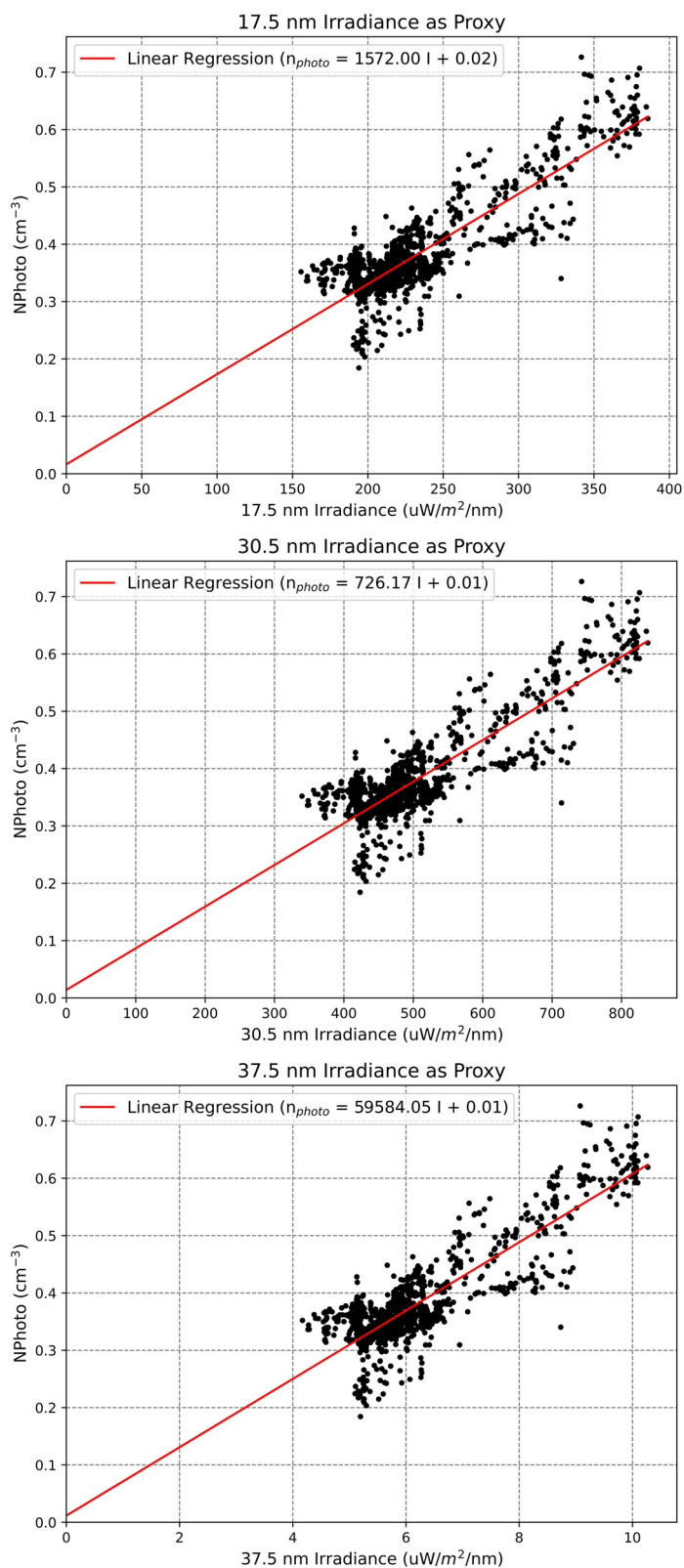


Figure A2. Scatterplots between n_{photo} estimates produced by the automated tool and irradiance data for three wavelengths reported as suitable proxies for the effective solar UV inducing the instrument effect. The red line is that of a linear regression between the data, and these were selected due to the strength of their fit as well as their small intercept term (required to make Equation 2 work).

the instrument aperture photoelectron emission level as single parameters correlated to a larger, more complex, changing solar EUV spectrum.

Data Availability Statement

MMS/FPI flight data used for this publication is available from the MMS Science Data Center, located online at <https://lasp.colorado.edu/mms/sdc/public/>. The SORCE/XPS, TIMED/SEE, and NOAA F10.7 cm Radio Flux irradiance data used for this publication is available for the Laboratory of Atmospheric and Space Physics (LASP) at CU Boulder, specifically the LASP Interactive Solar Irradiance Data Center (LISIRD), located online at <http://lasp.colorado.edu/lisird/>.

Acknowledgments

This research was supported by NASA funding to the MMS Fast Plasma Investigation (MMS/FPI). We thank all members of the MMS/FPI instrument team and the MMS community at large for their support while conducting this study.

References

- Bolton, S. J., Lunine, J., Stevenson, D., Connerney, J. E. P., Levin, S., Owen, T. C., et al. (2017). The Juno Mission. *Space Science Reviews*, 2131, 5–37. <https://doi.org/10.1007/s11214-017-0429-6>
- Brace, L. H., Hoegy, W. R., & Theis, R. F. (1988). Solar EUV measurements at Venus based on photoelectron emission from the Pioneer Venus Langmuir probe. *Journal of Geophysical Research*, 93, 7282–7296. <https://doi.org/10.1029/ja093ia07p07282>
- Burch, J. L., Moore, T. E., Torbert, R. B., & Giles, B. L. (2016). Magnetospheric multiscale overview and science objectives. *Space Science Reviews*, 199, 5–21. <https://doi.org/10.1007/s11214-015-0164-9>
- Del Zanna, G., & Andretta, V. (2011). The EUV spectrum of the Sun: SOHO CDS NIS irradiances from 1998 until 2010. *Astronomy & Astrophysics*, 528, A139. <https://doi.org/10.1051/0004-6361/201016106>
- Funsten, H. O., Skoug, R. M., Guthrie, A. A., MacDonald, E. A., Baldonado, J. R., Harper, R. W., et al. (2013). Helium, Oxygen, Proton, and Electron (HOPE) mass spectrometer for the radiation belt storm probes mission. *Space Science Reviews*, 179, 1423–1448. <https://doi.org/10.1007/s11214-013-9968-7>
- Gershman, D. J., Avakov, L. A., Boardsen, S. A., Dorelli, J. C., Gliese, U., Barrie, A. C., et al. (2017). Spacecraft and instrument photoelectrons measured by the dual electron spectrometers on MMS. *Journal of Geophysical Research: Space Physics*, 122, 11–548. <https://doi.org/10.1002/2017ja024518>
- Harris, F. K. (1948). New materials. *Review of Scientific Instruments*, 195, 379–380. <https://doi.org/10.1063/1.1741271>
- Kivelson, M. G., & Russell, C. T. (1997). Book review: Introduction to space physics/Cambridge U press. *Irish Astronomical Journal*, 24, 87.
- Lean, J. (1987). Solar ultraviolet irradiance variations: A review. *Journal of Geophysical Research*, 92(D1), 839–868. <https://doi.org/10.1029/jd092i01p00839>
- Lemen, J. R., Akin, D. J., Boerner, P. F., Chou, C., Drake, J. F., Duncan, D. W., et al. (2011). The atmospheric imaging assembly (AIA) on the solar dynamics observatory (SDO). In *The solar dynamics observatory* (pp. 17–40). Springer.
- Lybekk, B., Pedersen, A., Haaland, S., Svenes, K., Fazakerley, A. N., Masson, A., et al. (2012). Solar cycle variations of the Cluster spacecraft potential and its use for electron density estimations. *Journal of Geophysical Research*, 117(A1). <https://doi.org/10.1029/2011ja016969>
- Mahajan, K. K., Upadhyay, H. O., Sethi, N. K., Hoegy, W. R., Pesnell, W. D., & Brace, L. H. (1998). Pioneer Venus Orbiter measurements of solar EUV flux during solar cycles 21 and 22. In *Solar electromagnetic radiation study for Solar Cycle 22* (pp. 203–216). Dordrecht: Springer. https://doi.org/10.1007/978-94-011-5000-2_17
- Mauk, B. H., Fox, N. J., Kanekal, S. G., Kessel, R. L., Sibeck, D. G., & Ukhorskiy, A. A. (2013). Science objectives and rationale for the radiation belt Storm probes mission. *Space Science Reviews*, 179, 13–427. <https://doi.org/10.1007/s11214-012-9908-y>
- McComas, D. J., Alexander, N., Allegrini, F., Bagenal, F., Beebe, C., Clark, G., et al. (2017). The Jovian Auroral Distributions Experiment (JADE) on the Juno Mission to Jupiter. *Space Science Reviews*, 2131, 547–643. <https://doi.org/10.1007/s11214-013-9990-9>
- McFadden, J. P., Carlson, C. W., Larson, D., Ludlam, M., Abiad, R., Elliott, B., et al. (2008). The THEMIS ESA plasma instrument and in-flight calibration. *Space Science Reviews*, 141, 1277–1302. <https://doi.org/10.1007/s11214-008-9440-2>
- Mueller, D., Marsden, R. G., Cyr, O. S., & Gilbert, H. R. (2013). Solar orbiter. *Solar Physics*, 2851, 25–70.
- NOAA Space Weather Prediction Center (2021). *Solar EUV Irradiance* | NOAA/ NWS Space Weather Prediction Center. Retrieved From www.swpc.noaa.gov/phenomena/solar-euv-irradiance
- Owen, C. J., Bruno, R., Livi, S., Louarn, P., Al Janabi, K., Allegrini, F., et al. (2020). The Solar orbiter Solar Wind Analyser (SWA) suite. *Astronomy & Astrophysics*, 642, A16.
- Petrovay, K. (2020). Solar cycle prediction. *Living Reviews in Solar Physics*, 171, 1–93. <https://doi.org/10.1007/s41116-020-0022-z>
- Pollock, C., Moore, T., Jacques, A., Burch, J., Gliese, U., Saito, Y., et al. (2016). Fast plasma investigation for magnetospheric multiscale. *Space Science Reviews*, 199, 331–406.
- Priest, E. R. (2012). *Solar Magnetohydrodynamics* (Vol. 21). Springer Science & Business Media.
- Rottman, G. J. (1988). Observations of solar UV and EUV variability. *Advances in Space Research*, 87, 53–66. [https://doi.org/10.1016/0273-1177\(88\)90172-x](https://doi.org/10.1016/0273-1177(88)90172-x)
- Torkar, K., Nakamura, R., Tajmar, M., Scharlemann, C., Jeszenszky, H., Laky, G., et al. (2016). Active spacecraft potential control investigation. *Space Science Reviews*, 199, 515–544. <https://doi.org/10.1007/s11214-014-0049-3>